

# Nonlocal Patch-Based Fully-Connected Tensor Network Decomposition for Remote Sensing Image Inpainting

Wen-Jie Zheng, Xi-Le Zhao, Yu-Bang Zheng, and Zhi-Feng Pang

**Abstract**—Remote sensing image (RSI) inpainting plays an important role in real applications. Recently, fully-connected tensor network (FCTN) decomposition has been shown the remarkable ability to fully characterize the global correlation. Considering the global correlation and the nonlocal self-similarity (NSS) of RSIs, this paper introduces the FCTN decomposition to the whole RSI and its NSS groups, and proposes a novel nonlocal patch-based FCTN (NL-FCTN) decomposition for RSI inpainting. Different from other nonlocal patch-based methods, the NL-FCTN decomposition-based method, which increases tensor order by stacking similar small-sized patches to NSS groups, cleverly leverages the remarkable ability of FCTN decomposition to deal with higher-order tensors. Besides, we propose an efficient proximal alternating minimization-based algorithm to solve the proposed NL-FCTN decomposition-based model with a theoretical convergence guarantee. Extensive experiments on RSIs demonstrate that the proposed method achieves the state-of-the-art inpainting performance in all compared methods.

**Index Terms**—Remote sensing image (RSI) inpainting, nonlocal self-similarity (NSS), tensor order increment, fully-connected tensor network (FCTN) decomposition.

## I. INTRODUCTION

REMOTE sensing images (RSIs) contain a wealth of spatial, spectral, and temporal information, which makes them widely applied in various applications [1]–[3]. In practice, however, RSIs obtained are often incomplete due to some unavoidable factors, such as dead pixels and cloud cover. In order to improve the subsequent practicability, it is important to estimate missing elements by RSI inpainting [4]–[6]. The core problem of RSI inpainting is to characterize the intrinsic prior of RSIs [7]–[10].

Global correlation is an important prior of RSIs. Since RSIs are usually modeled as higher-order tensors, whose global correlation can be captured by tensor decomposition. There are various types of tensor decomposition, such as CANDECOMP/PARAFAC (CP) decomposition, Tucker decomposition, tensor singular value decomposition (t-SVD),

tensor train (TT) decomposition, and tensor ring (TR) decomposition. All of them have been increasingly applied to RSI restoration and achieved promising results. For example, Liu et al. [11] proposed a CP decomposition-based RSI denoising model, and Ng et al. [12] introduced a Tucker decomposition-based adaptive weighted sum of the nuclear norm (SNN) for RSI inpainting. Based on t-SVD, Fan et al. [13] employed tensor nuclear norm (TNN) to RSI restoration, and Zheng et al. [14] further expanded TNN to convex three-directional tensor nuclear norm and non-convex three-directional log-based tensor nuclear norm, and proposed two models for mixed noise removal. TT and TR decompositions as two representative tensor network decompositions received extensive applications in image restoration, since they have the superior capability to deal with higher-order tensors. For example, Bengua et al. [15] first proposed a TT decomposition-based image inpainting model, and Ding et al. [16] further embedded a total variation (TV) regularization into TT decomposition to improve the capability of image details recovery. Based on TR decomposition, Yuan et al. [17] and He et al. [18] proposed an image inpainting method by combining factor regularization and TV regularization, respectively.

However, the methods directly considered the global correlation, which ignored the redundancy of repeated local patches across the spatial modes of RSIs, i.e., nonlocal self-similarity (NSS). One way to fully utilize NSS prior is to apply tensor low-rank method, such as log-based SNN [19] and TNN, to each NSS group [20], which is a new tensor obtained by stacking similar small-sized patches. By taking a third-order multispectral image (MSI) as an example, each original NSS group is a fourth-order tensor, including two spatial modes, one spectral mode, and one similar-group mode. However, traditional methods usually reshaped two spatial modes in each NSS group to one mode, which cannot better preserve the spatial structure of each NSS group. Therefore, Ding et al. [21] exploited TT rank minimization to the original fourth-order NSS groups and achieved promising completion results. But TT decomposition only characterizes the correlation between adjacent two modes, causing a limited characterization for the NSS groups.

Recently, a fully-connected tensor network (FCTN) decomposition has been proposed, which establishes an operation between any two modes and has the powerful capability to capture the global correlation of tensors [22]. Based on FCTN decomposition, this paper makes two-fold contributions listing as follows:

This work was supported in part by the National Natural Science Foundation of China under Grant 61876203 and Grant 12071345, in part by the Project for Applied Basic Research of Sichuan Province under Grant 2021YJ0107, and in part by the Program for Science and Technology Development of Henan Province under Grant 212102210511. (Corresponding authors: Xi-Le Zhao and Yu-Bang Zheng.)

W.-J. Zheng, X.-L. Zhao, and Y.-B. Zheng are with the School of Mathematical Sciences, University of Electronic Science and Technology of China, Chengdu 611731, China (e-mail: wjz1355@163.com; xilzhao122003@163.com; zhengyubang@163.com).

Z.-F. Pang is with the School of Mathematics and Statistics, Henan University, Kaifeng 475004, China (e-mail: zhifengpang@163.com).

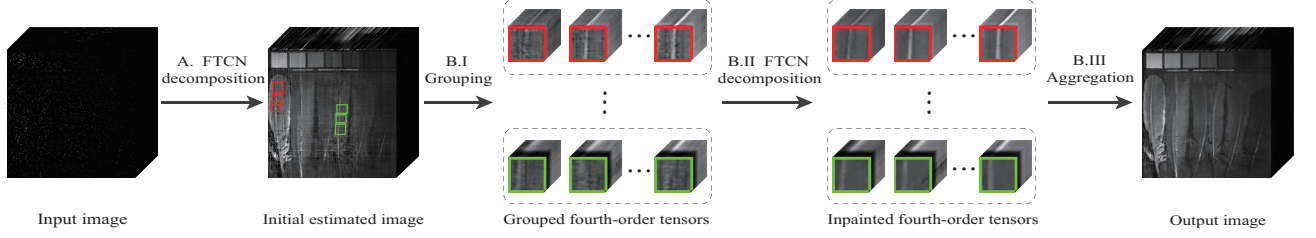


Fig. 1. Flowchart of the proposed RSI inpainting method. It involves two stages: A. initial FCTN decomposition inpainting and B. nonlocal FCTN decomposition inpainting. B includes three steps consisted of grouping, grouped FCTN decomposition inpainting, and aggregation.

TABLE I  
NOTATION DECLARATIONS.

| Notations                                | Interpretations  |
|--|--|
| $x, \mathbf{x}, \mathbf{X}, \mathcal{X}$ | scalar, vector, matrix, tensor   |
| $\mathcal{X}(i_1, i_2, \dots, i_N)$      | the $(i_1, i_2, \dots, i_N)$ th element of $\mathcal{X}$                                       |
| $\mathcal{X}_{1:d}$                      | $(\mathcal{X}_1, \mathcal{X}_2, \dots, \mathcal{X}_d)$   |
| $\ \mathcal{X}\ _F$                      | $\ \mathcal{X}\ _F = \sqrt{\sum_{i_1, i_2, \dots, i_N}  \mathcal{X}(i_1, i_2, \dots, i_N) ^2}$ |

First, we suggest a novel nonlocal patch-based FCTN (NL-FCTN) decomposition-based RSI inpainting model, the flowchart of which is illustrated in Fig 1. As shown in Fig 1, the proposed model has two advantages. On the one hand, employing FCTN decomposition to the whole RSI and its NSS groups fully develops the global correlation and the NSS of RSIs. On the other hand, NL-FCTN decomposition-based method regards the process of stacking similar small-sized patches to NSS groups as a tensor order increment operation, which cleverly leverages the remarkable ability of FCTN decomposition on dealing with higher-order tensors.

Second, we develop a proximal alternating minimization (PAM)-based algorithm to solve the NL-FCTN decomposition-based model with a theoretical guarantee of convergence. Extensive experiments show that the proposed method outperforms the state-of-the-art methods on RSI inpainting.

## II. NOTATIONS AND PRELIMINARIES

We summarize the notations throughout this paper in Table I, and introduce a generalized tensor unfolding operation following [22]. Supposing that  $\mathbf{n}$  is a reordering of the vector  $(1, 2, \dots, N)$ , the generalized tensor unfolding represents an  $N$ th-order tensor  $\mathcal{X} \in \mathbb{R}^{I_1 \times I_2 \times \dots \times I_N}$  as a matrix  $\mathbf{X} \in \mathbb{R}^{\prod_{i=1}^d I_{n_i} \times \prod_{i=d+1}^N I_{n_i}}$ , which is denoted by  $\mathbf{X}_{[n_{1:d}; n_{d+1:N}]} = \text{GenUnfold}(\mathcal{X}, n_{1:d}; n_{d+1:N})$ . On the contrary, its inverse operation is denoted by  $\mathcal{X} = \text{GenFold}(\mathbf{X}_{[n_{1:d}; n_{d+1:N}]}, n_{1:d}; n_{d+1:N})$ .

## III. PROPOSED RSI INPAINTING METHOD

In this section, we start with a brief introduction to the definition and properties of FCTN decomposition, and then introduce the proposed NL-FCTN decomposition-based method for RSI inpainting in detail.

### A. FCTN Decomposition

Compared with TT and TR decompositions, FCTN decomposition is more efficient and more genreal. Specifically, by factorizing an  $N$ th-order tensor into a sequence of small-sized  $N$ th-order factor tensors and establishing the relationship between any two factors, FCTN decomposition has the remarkable ability to fully characterize the global correlation of tensors. Mathematically, given an  $N$ th-order tensor  $\mathcal{X} \in \mathbb{R}^{I_1 \times I_2 \times \dots \times I_N}$ , FCTN decomposition denotes each element of  $\mathcal{X}$  by

$$\begin{aligned} \mathcal{X}(i_1, i_2, \dots, i_N) = & \sum_{r_{1,2}=1}^{R_{1,2}} \sum_{r_{1,3}=1}^{R_{1,3}} \dots \sum_{r_{1,N}=1}^{R_{1,N}} \sum_{r_{2,3}=1}^{R_{2,3}} \sum_{r_{2,N}=1}^{R_{2,N}} \dots \sum_{r_{N-1,N}=1}^{R_{N-1,N}} \\ & \{ \mathcal{G}_1(i_1, r_{1,2}, r_{1,3}, \dots, r_{1,N}) \\ & \mathcal{G}_2(r_{1,2}, i_2, r_{2,3}, \dots, r_{2,N}) \dots \\ & \mathcal{G}_k(r_{1,k}, r_{2,k}, \dots, r_{k-1,k}, i_k, r_{k,k+1}, \dots, r_{k,N}) \dots \\ & \mathcal{G}_N(r_{1,N}, r_{2,N}, \dots, r_{N-1,N}, i_N) \}, \end{aligned} \quad (1)$$

where  $\mathcal{G}_k \in \mathbb{R}^{R_{1,k} \times R_{2,k} \times \dots \times R_{k-1,k} \times I_k \times R_{k,k+1} \times \dots \times R_{k,N}}$  ( $k = 1, 2, \dots, N$ ) are called the FCTN-factors and the vector  $(R_{1,2}, R_{1,3}, \dots, R_{1,N}, R_{2,3}, \dots, R_{2,N}, \dots, R_{N-1,N})$  is called the FCTN-rank. For the sake of simplicity, the equation (1) can be expressed as  $\mathcal{X} = \text{FCTN}(\mathcal{G}_1, \mathcal{G}_2, \dots, \mathcal{G}_N)$ .

Fig. 2 vividly illustrates the graphic structure of FCTN decomposition. In Fig. 2, we can clearly observe that any two FCTN factors are linked by a line, representing a multi-linear operation between them.

### B. NL-FCTN Decomposition-Based RSI Inpainting Method

The following is a detailed derivation of the proposed NL-FCTN decomposition-based model for RSI inpainting with the Fig.1. The model consists of two stages. In stage A, we introduce FCTN decomposition to the whole RSI as an initialization process, guaranteeing the high accuracy of the subsequent group matching.

In stage B, there are three steps. In step B.I, we divide the initial RSI into small-sized patches, and stack similar patches as NSS groups. By taking an MSI  $\mathcal{F} \in \mathbb{R}^{I_1 \times I_2 \times I_3}$  as an example, we divide it into overlapped cubes  $\{\mathcal{F}_t \in \mathbb{R}^{p \times p \times I_3}\}_{t=1}^T$  with patch size  $p$ , where  $T = ((I_1 - p)/(p - o) + 1) \times ((I_2 - p)/(p - o) + 1)$  is the number of total patches and  $o$  is the size of overlap. Then, we select key patches from total patches with a fixed interval of  $v$ .  $L = ((I_1 - p)/v + 1) \times ((I_2 - p)/v + 1)$  is the

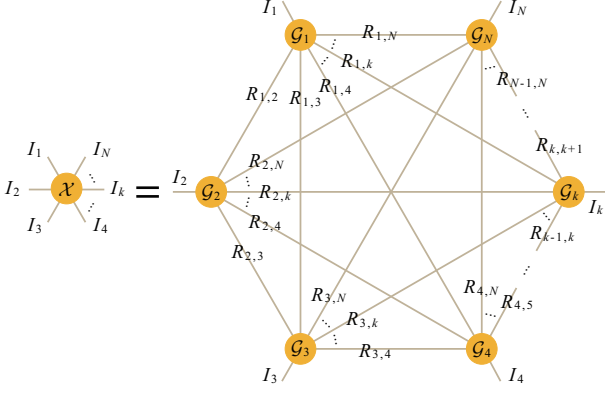


Fig. 2. Illustration of FCTN decomposition.

number of key patches as well as the number of NSS groups. This is because an NSS group consists of cubes stacking by a key patch and its similar patches. For each key patch, its similar patches are obtained by block matching. The way is to utilize the Euclidean distance to access similarity between each key patch and all total patches, and cluster the first  $s$  similar patches into an NSS group. The NSS groups of MSI are denoted by  $\{\hat{\mathcal{F}}_l \in \mathbb{R}^{p \times p \times I_3 \times s}\}_{l=1}^L$ . Thus, a third-order MSI  $\mathcal{F}$  transforms into a set of fourth-order NSS groups  $\{\hat{\mathcal{F}}_l\}_{l=1}^L$  by group matching. Following a similar step described above, a fourth-order time-series RSI with the size of  $I_1 \times I_2 \times I_3 \times I_4$  transforms into a set of fifth-order NSS groups with the size of  $p \times p \times I_3 \times I_4 \times s$ . More generally, an  $N$ th-order tensor naturally transforms into a set of  $(N+1)$ th-order NSS groups.

In step B.II, we regard an NSS group as a basis inpainting unit because of its strong global correlation, and introduce FCTN decomposition to each NSS group. For FCTN decomposition, this step not only makes full use of the remarkable ability to characterize the global correlation, but also cleverly leverages the advantage of dealing with higher-order tensors by NSS-based tensor order increment operation.

Without loss of generality, we consider an  $(N+1)$ th-order NSS group  $\hat{\mathcal{F}}_l$  and employ FCTN decomposition to obtain the inpainted NSS group  $\hat{\mathcal{X}}_l$ , which can be formulated as

$$\begin{aligned} \min_{\hat{\mathcal{X}}_l, \mathcal{G}} \quad & \frac{1}{2} \|\hat{\mathcal{X}}_l - \text{FCTN}(\mathcal{G}_1, \mathcal{G}_2, \dots, \mathcal{G}_{N+1})\|_F^2 \\ \text{s.t.} \quad & \mathcal{P}_{\Omega_l}(\hat{\mathcal{X}}_l) = \mathcal{P}_{\Omega_l}(\hat{\mathcal{F}}_l), \end{aligned} \quad (2)$$

where  $\mathcal{P}_{\Omega_l}(\cdot)$  is the projection operator that keeps the entries in  $\Omega_l$  and sets others to zero, and  $\Omega_l$  is the index of known elements in  $\hat{\mathcal{F}}_l$ . Since (2) is convex for  $\hat{\mathcal{X}}_l$  and the FCTN-factors  $\mathcal{G}_i (i = 1, 2, \dots, N+1)$  independently, PAM [23] is introduced to obtain the solution as follows:

$$\begin{cases} \mathcal{G}_i^{(q+1)} = \underset{\mathcal{G}_i}{\text{argmin}} \left\{ \frac{1}{2} \|\hat{\mathcal{X}}_l^{(q)} - \text{FCTN}(\mathcal{G}_{1:i-1}^{(q+1)}, \mathcal{G}_i, \mathcal{G}_{i+1:N+1}^{(q)})\|_F^2 \right. \\ \quad \left. + \frac{\rho}{2} \|\mathcal{G}_i - \mathcal{G}_i^{(q)}\|_F^2 \right\}, \quad i = 1, 2, \dots, N+1, \\ \hat{\mathcal{X}}_l^{(q+1)} = \underset{\mathcal{P}_{\Omega_l}(\hat{\mathcal{X}}_l) = \mathcal{P}_{\Omega_l}(\hat{\mathcal{F}}_l)}{\text{argmin}} \left\{ \frac{1}{2} \|\hat{\mathcal{X}}_l - \text{FCTN}(\mathcal{G}_{1:N+1}^{(q+1)})\|_F^2 \right. \\ \quad \left. + \frac{\rho}{2} \|\hat{\mathcal{X}}_l - \hat{\mathcal{X}}_l^{(q)}\|_F^2 \right\}, \end{cases} \quad (3)$$

### Algorithm 1 PAM-Based Algorithm for NL-FCTN Decomposition-Based RSI Inpainting Model

**Input:** The degraded RSI  $\mathcal{T} \in \mathbb{R}^{I_1 \times I_2 \times \dots \times I_N}$ , the index set  $\Omega$ , the patch size  $p$ , the similar patch number  $s$ , and the FCTN-rank  $R$ .  
**Initialization:** The initial iterations  $q = 0$ , the maximum iterations  $q_{\max} = 100$ , the overlapped patch size  $o = 1$ , the key patch interval  $v = p - 1$ , and  $\rho = 0.01$ .

- 1: **Stage A. initial FCTN decomposition inpainting**
- 2: Inpaint the degraded RSI  $\mathcal{T}$  via FCTN decomposition and obtain an initial RSI  $\mathcal{F}$ .
- 3: **Stage B. nonlocal FCTN decomposition inpainting**
- 4: (I) Group similar patches over all bands of  $\mathcal{F}$  and obtain a set of  $(N+1)$ th-order NSS groups  $\{\hat{\mathcal{F}}_l\}_{l=1}^L$ .
- 5: (II) Inpaint each NSS group  $\hat{\mathcal{F}}_l$  via FCTN decomposition
- 6: **for**  $l = 1 : L$  **do**
- 7:     Update  $\hat{\mathcal{F}}_l$  via (5) and obtain  $\hat{\mathcal{X}}_l$ .
- 8: **end for**
- 9: (III) Aggregate the inpainted NSS groups  $\{\hat{\mathcal{X}}_l\}_{l=1}^L$  to form the inpainted RSI  $\mathcal{X}$ .

**Output:** The inpainted RSI  $\mathcal{X}$ .

where  $\mathcal{G}_i^{(q)} (i = 1, 2, \dots, N+1)$  and  $\hat{\mathcal{X}}_l^{(q)}$  are the results of the  $q$ th iteration of  $\mathcal{G}_i (i = 1, 2, \dots, N+1)$  and  $\hat{\mathcal{X}}_l$  respectively, and  $\rho > 0$  is a proximal parameter. According to Theorem 4 in [22],

$$\hat{\mathbf{X}}_{l(i)} = (\mathbf{G}_i)_{(i)} (\mathbf{M}_i)_{[m_{1:N}; n_{1:N}]},$$

where  $\mathcal{M}_i = \text{FCTN}(\{\mathcal{G}_j\}_{j=1}^{N+1}, / \mathcal{G}_i)$  is a composition of  $\mathcal{G}_1, \mathcal{G}_2, \dots, \mathcal{G}_{i-1}, \mathcal{G}_{i+1}, \dots, \mathcal{G}_{N+1}$ ,

$$m_j = \begin{cases} 2j, & \text{if } j < i, \\ 2j-1, & \text{if } j \geq i, \end{cases} \quad \text{and} \quad n_j = \begin{cases} 2j-1, & \text{if } j < i, \\ 2j, & \text{if } j \geq i. \end{cases}$$

Thus, the  $\mathcal{G}_i (i = 1, 2, \dots, N+1)$ -subproblems are given by

$$\begin{aligned} \mathcal{G}_i^{(q+1)} = \underset{\mathcal{G}_i}{\text{argmin}} \left\{ \frac{\rho}{2} \|\mathcal{G}_i - \mathcal{G}_i^{(q)}\|_F^2 \right. \\ \left. + \frac{1}{2} \|\hat{\mathbf{X}}_{l(i)}^{(q)} - (\mathbf{G}_i)_{(i)} (\mathbf{M}_i^{(q)})_{[m_{1:N}; n_{1:N}]} \|^2 \right\}. \end{aligned} \quad (4)$$

It is easy to find that (3) and (4) have the closed-form solutions as

$$\begin{cases} \mathcal{G}_i^{(q+1)} = \text{GenFold} \left( [\hat{\mathbf{X}}_{l(i)}^{(q)} (\mathbf{M}_i^{(q)})_{[n_{1:N}; m_{1:N}]} + \rho (\mathbf{G}_i^{(q)})_{(i)}] \right. \\ \quad \left. [(\mathbf{M}_i^{(q)})_{[m_{1:N}; n_{1:N}]} (\mathbf{M}_i^{(q)})_{[n_{1:N}; m_{1:N}]} + \rho \mathbf{I}]^{-1} \right), \\ \quad \quad \quad i = 1, 2, \dots, N+1, \\ \hat{\mathcal{X}}_l^{(q+1)} = \mathcal{P}_{\Omega_l} \left( \frac{\text{FCTN}(\{\mathcal{G}_i^{(q+1)}\}_{i=1}^{N+1}) + \rho \hat{\mathcal{X}}_l^{(q)}}{1 + \rho} \right) + \mathcal{P}_{\Omega_l}(\hat{\mathcal{F}}_l). \end{cases} \quad (5)$$

In step B.III, we aggregate the inpainted NSS groups  $\{\hat{\mathcal{X}}_l\}_{l=1}^L$  to their original positions and obtain the whole inpainted RSI  $\mathcal{X}$ .

The above NL-FCTN decomposition-based method for RSI inpainting is summarized in Algorithm 1. Its theoretical convergence can be similarly proved following [22].

## IV. NUMERICAL EXPERIMENTS

In this section, we test the performance of NL-FCTN decomposition-based method for RSI inpainting on the MSIs (third-order tensors) and the time-series sentinel-2 images



TABLE II  
THE AVERAGE PSNR, SSIM, AND SAM VALUES ON ALL TESTING MSIS OF SIX UTILIZED METHODS.

| MR      | 98%            |               |                | 95%            |               |               | 90%            |               |               | 80%            |               |               |
|---------|----------------|---------------|----------------|----------------|---------------|---------------|----------------|---------------|---------------|----------------|---------------|---------------|
| Method  | PSNR           | SSIM          | SAM            | PSNR           | SSIM          | SAM           | PSNR           | SSIM          | SAM           | PSNR           | SSIM          | SAM           |
| KBR-TC  | 22.6409        | 0.6428        | 20.4000        | 33.5480        | 0.9110        | 6.8097        | 41.7296        | 0.9774        | 3.4463        | 48.5367        | 0.9941        | 1.9720        |
| NL-SNN  | 16.5703        | 0.6420        | 17.9006        | 29.6485        | 0.8645        | 6.1118        | 41.3033        | 0.9774        | 2.5377        | 47.3655        | 0.9914        | 1.7127        |
| NL-TNN  | 19.8220        | 0.6568        | 26.3135        | 31.6988        | 0.9219        | 8.6298        | 36.7736        | 0.9704        | 3.9475        | 44.1860        | 0.9930        | 1.7618        |
| NL-TT   | 26.3712        | 0.7862        | 15.2674        | 31.4861        | 0.9051        | 6.6808        | 34.7360        | 0.9472        | 3.9148        | 38.4261        | 0.9752        | 2.5169        |
| FCTN-TC | 25.9944        | 0.6625        | 19.1886        | 33.0224        | 0.8631        | 9.8324        | 37.7269        | 0.9373        | 6.6739        | 43.6822        | 0.9760        | 4.2126        |
| NL-FCTN | <b>28.4943</b> | <b>0.8042</b> | <b>11.9528</b> | <b>37.5379</b> | <b>0.9596</b> | <b>3.9858</b> | <b>44.2862</b> | <b>0.9901</b> | <b>2.0703</b> | <b>49.7174</b> | <b>0.9964</b> | <b>1.3360</b> |

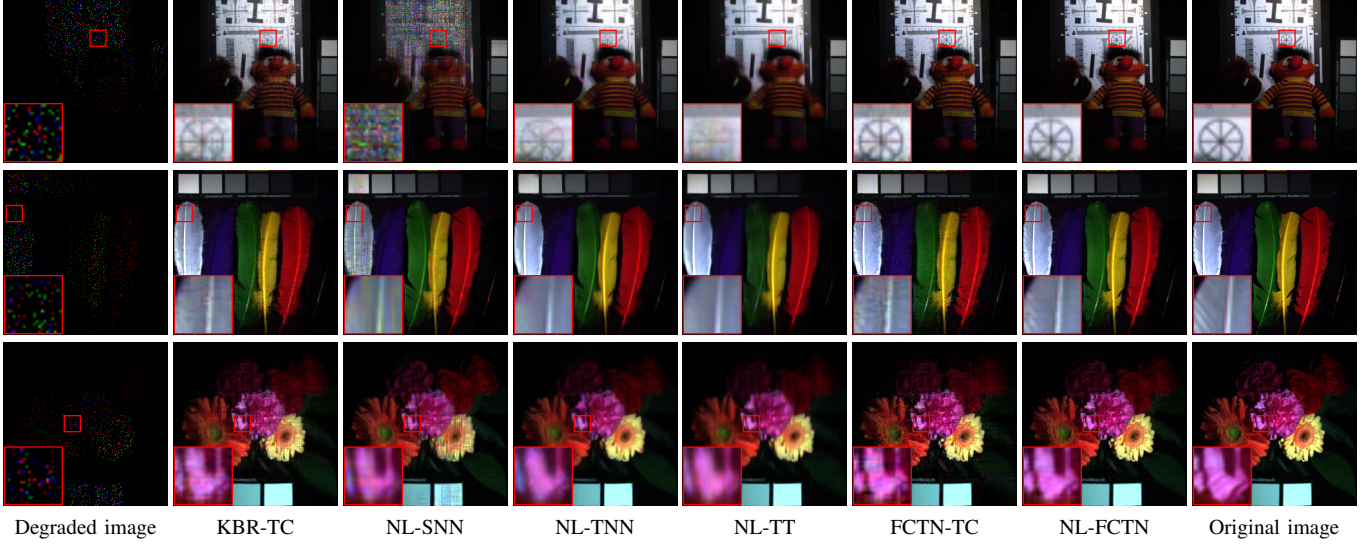


Fig. 3. Restoration results of three selected MSIs with MR=95%. The pseudo color images are composed of bands 29, 14, and 5. From top to bottom: the results of *chart* and *stuffed toy*, *feathers*, and *flowers*.

(fourth-order tensors). The compared methods are global tensor decomposition-based tensor completion (TC) methods including KBR-TC [24] and FCTN-TC [22], and nonlocal patch-based tensor decomposition for TC including NL-SNN [19], NL-TNN [20], and NL-TT [21]. All hyper-parameters of each compared method are set for the optimal performance according to the authors' paper and code. Three quantitative metrics contain the peak signal to noise rate (PSNR), the structural similarity (SSIM), and the spectral angle mapping (SAM).

1) *MSI Inpainting*: We test the CAVE Database<sup>1</sup> with 32 MSIs. Each test MSI is resized to  $256 \times 256 \times 31$  and rescaled to  $[0,1]$ . The missing rate (MR) is defined as the rate of the unknown elements in the total elements. We test four MRs: 98%, 95%, 90%, and 80%. Table II reports the average values of PSNR, SSIM, and SAM on all 32 MSIs by six compared methods under each MR. We observe that the proposed method performs better than the compared methods for all quantitative metrics. Particularly, our method is around 4 dB higher than the second best performed method with MR=95%. Compared with other methods, we also observe that KBR-TC, NL-SNN, and NL-TNN perform well with low MR and perform poorly with high MR; NL-TT performs poorly with low MR and performs well with high MR; FCTN-TC shows moderate but stable performance. Naturally, NL-FCTN introduces FCTN-

TC to the whole MSI and its NSS groups, which achieves the best performance.

Fig. 3 shows the pseudo color images of restoration results with MR=95% of three MSIs. As observed, the proposed method achieves superior inpainting results visually. In particular, the spatial textures of MSIs can be better preserved, such as the lines in *feathers* and the petals in *flowers*.

2) *Time-Series Sentinel-2 Image Cloud Removal*: The time-series sentinel-2 image, named *Morocco*<sup>2</sup>, is taken over Morocco, which is resized to  $200 \times 200 \times 4 \times 6$  and rescaled to  $[0,1]$ . To simulate the real scene, we assume that all bands of *Morocco* at the same time node are covered by the same type of clouds and at different time nodes are covered by different types of clouds. Table III reports the PSNR, SSIM, and SAM on cloud removal results of *Morocco* by all compared methods. We observe that the proposed method achieves better results regardless of RSNR, SSIM, or SAM.

Fig. 4 shows the pseudo images of cloud removal results of *Morocco* at two time nodes. Especially in the red box, we observe that KBR-TC can not better preserve the spectral information and causes color loss; NL-SNN, NL-TNN, and NL-TT blur the detail textures of the spatial images; FCTN-TC preserves the details but causes some artifacts; NL-FCTN achieves the closest restoration to the original images among all compared methods.

<sup>1</sup><https://www.cs.columbia.edu/CAVE/databases/multispectral/>.

<sup>2</sup><https://theia.cnes.fr/atdistrib/rocket/#/home>.



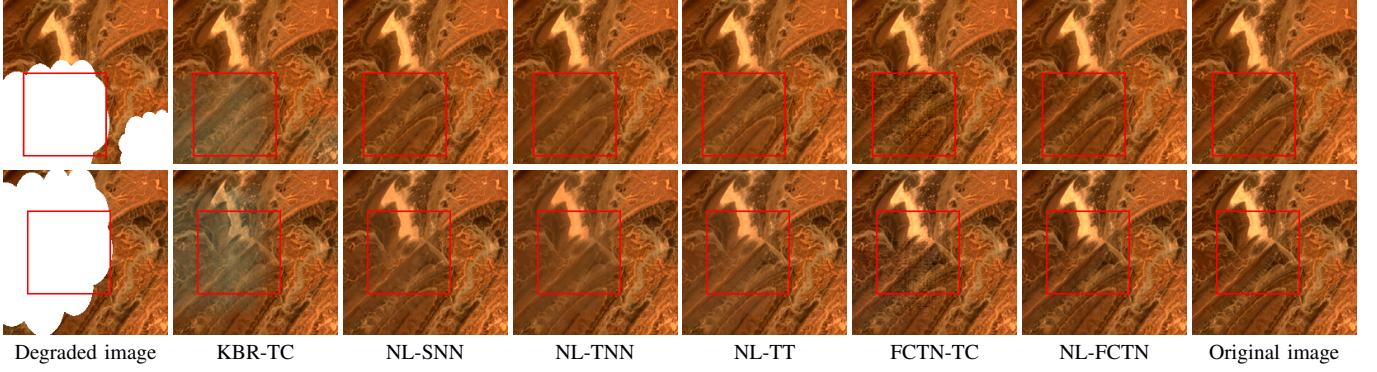


Fig. 4. Cloud removal results of *Morocco*. The pseudo color images are composed of bands 3, 2, and 1. From top to bottom: the results at the second time node and the fourth time node.

TABLE III  
THE PSNR, SSIM, AND SAM VALUES ON MOROCCO OF SIX UTILIZED METHODS.

| Method  | PSNR           | SSIM          | SAM           |
|---------|----------------|---------------|---------------|
| KBR-TC  | 33.8532        | 0.9707        | 2.7453        |
| NL-SNN  | 46.8914        | 0.9888        | 0.3367        |
| NL-TNN  | 43.0896        | 0.9810        | 0.4468        |
| NL-TT   | 39.7771        | 0.9073        | 1.2499        |
| FCTN-TC | 44.1284        | 0.9826        | 0.3633        |
| NL-FCTN | <b>48.1321</b> | <b>0.9945</b> | <b>0.2436</b> |

## V. CONCLUSION

In this paper, we proposed an NL-FCTN decomposition-based method for RSI inpainting. We introduced FCTN decomposition to the whole RSI and its NSS groups to fully characterize the global correlation and the NSS of RSIs. From another perspective, we combined the FCTN decomposition with the nonlocal patch-based tensor order increment operation, which cleverly leverages its remarkable ability on higher-order tensors. The NL-FCTN decomposition-based model was solved by a PAM-based algorithm with a theoretical convergence guarantee. Extensive experiments proved that the proposed method performed better than all compared methods.

## REFERENCES

- [1] W. Sun, G. Yang, J. Peng, and Q. Du, "Lateral-slice sparse tensor robust principal component analysis for hyperspectral image classification," *IEEE Geosci. Remote Sens. Lett.*, vol. 17, no. 1, pp. 107–111, 2019.
- [2] D. Hong, J. Chanussot, N. Yokoya, J. Kang, and X. X. Zhu, "Learning-shared cross-modality representation using multispectral-lidar and hyperspectral data," *IEEE Geosci. Remote Sens. Lett.*, vol. 17, no. 8, pp. 1470–1474, 2020.
- [3] D. Hong, W. He, N. Yokoya, J. Yao, L. Gao, L. Zhang, J. Chanussot, and X. Zhu, "Interpretable hyperspectral artificial intelligence: When nonconvex modeling meets hyperspectral remote sensing," *IEEE Geosci. Remote Sens. Mag.*, vol. 9, no. 2, pp. 52–87, 2021.
- [4] M. Wang, Q. Wang, J. Chanussot, and D. Hong, "Total variation regularized weighted tensor ring decomposition for missing data recovery in high-dimensional optical remote sensing images," *IEEE Geosci. Remote Sens. Lett.*, pp. 1–5, 2021.
- [5] Q. Yuan, Q. Zhang, J. Li, H. Shen, and L. Zhang, "Hyperspectral image denoising for remote sensing images with unidirectional total variation and sparse representation," *IEEE Trans. Geosci. Remote Sens.*, vol. 57, no. 2, pp. 1205–1218, 2018.
- [6] Y. Chang, L. Yan, H. Fang, and H. Liu, "Simultaneous destriping and denoising for remote sensing images with unidirectional total variation and sparse representation," *IEEE Geosci. Remote Sens. Lett.*, vol. 11, no. 6, pp. 1051–1055, 2013.
- [7] W. He, Q. Yao, C. Li, N. Yokoya, and Q. Zhao, "Non-local meets global: An integrated paradigm for hyperspectral denoising," in *Proc. CVPR*, 2019, pp. 6868–6877.
- [8] Q. Zhang, Q. Yuan, J. Li, X. Liu, H. Shen, and L. Zhang, "Hybrid noise removal in hyperspectral imagery with a spatial-spectral gradient network," *IEEE Trans. Geosci. Remote Sens.*, vol. 57, no. 10, pp. 7317–7329, 2019.
- [9] L. Zhuang, X. Fu, M. K. Ng, and J. M. Bioucas-Dias, "Hyperspectral image denoising based on global and nonlocal low-rank factorizations," *IEEE Trans. Geosci. Remote Sens.*, pp. 1–17, 2021.
- [10] L. Zhuang, L. Gao, B. Zhang, X. Fu, and J. M. Bioucas-Dias, "Hyperspectral image denoising and anomaly detection based on low-rank and sparse representations," *IEEE Trans. Geosci. Remote Sens.*, pp. 1–17, 2020.
- [11] X. Liu, S. Bourennane, and C. Fossati, "Denoising of hyperspectral images using the parafac model and statistical performance analysis," *IEEE Trans. Geosci. Remote Sens.*, vol. 50, no. 10, pp. 3717–3724, 2012.
- [12] M. K.-P. Ng, Q. Yuan, L. Yan, and J. Sun, "An adaptive weighted tensor completion method for the recovery of remote sensing images with missing data," *IEEE Trans. Geosci. Remote Sens.*, vol. 55, no. 6, pp. 3367–3381, 2017.
- [13] H. Fan, Y. Chen, Y. Guo, H. Zhang, and G. Kuang, "Hyperspectral image restoration using low-rank tensor recovery," *IEEE J. Sel. Top. Appl. Earth Obs. Remote Sens.*, vol. 10, no. 10, pp. 4589–4604, 2017.
- [14] Y.-B. Zheng, T.-Z. Huang, X.-L. Zhao, T.-X. Jiang, T.-H. Ma, and T.-Y. Ji, "Mixed noise removal in hyperspectral image via low-fibered-rank regularization," *IEEE Trans. Geosci. Remote Sens.*, vol. 58, no. 1, pp. 734–749, 2019.
- [15] J. A. Bengua, H. N. Phien, H. D. Tuan, and M. N. Do, "Efficient tensor completion for color image and video recovery: Low-rank tensor train," *IEEE Trans. Image Process.*, vol. 26, no. 5, pp. 2466–2479, 2017.
- [16] M. Ding, T.-Z. Huang, T.-Y. Ji, X.-L. Zhao, and J.-H. Yang, "Low-rank tensor completion using matrix factorization based on tensor train rank and total variation," *J. Sci. Comput.*, vol. 81, no. 2, pp. 941–964, 2019.
- [17] L. Yuan, C. Li, D. Mandic, J. Cao, and Q. Zhao, "Tensor ring decomposition with rank minimization on latent space: An efficient approach for tensor completion," in *Proc. AAAI*, vol. 33, no. 1, 2019, pp. 9151–9158.
- [18] W. He, N. Yokoya, L. Yuan, and Q. Zhao, "Remote sensing image reconstruction using tensor ring completion and total variation," *IEEE Trans. Geosci. Remote Sens.*, vol. 57, no. 11, pp. 8998–9009, 2019.
- [19] T. Xie, S. Li, L. Fang, and L. Liu, "Tensor completion via nonlocal low-rank regularization," *IEEE Trans. Cybern.*, vol. 49, no. 6, pp. 2344–2354, 2018.
- [20] L. Song, B. Du, L. Zhang, L. Zhang, J. Wu, and X. Li, "Nonlocal patch based t-svd for image inpainting: Algorithm and error analysis," in *Proc. AAAI*, vol. 32, no. 1, 2018, pp. 2419–2426.
- [21] M. Ding, T.-Z. Huang, X.-L. Zhao, M. K. Ng, and T.-H. Ma, "Tensor train rank minimization with nonlocal self-similarity for tensor completion," *Inverse Probl. Imag.*, vol. 15, no. 3, 2021.
- [22] Y.-B. Zheng, T.-Z. Huang, X.-L. Zhao, Q. Zhao, and T.-X. Jiang, "Fully-connected tensor network decomposition and its application to higher-order tensor completion," in *Proc. AAAI*, vol. 35, no. 12, 2021, pp. 11 071–11 078.
- [23] H. Attouch, J. Bolte, and B. F. Svaiter, "Convergence of descent methods for semi-algebraic and tame problems: proximal algorithms, forward-backward splitting, and regularized gauss-seidel methods," *Math. Program.*, vol. 137, no. 1, pp. 91–129, 2013.
- [24] Q. Xie, Q. Zhao, D. Meng, and Z. Xu, "Kronecker-basis-representation based tensor sparsity and its applications to tensor recovery," *IEEE Trans. Pattern Anal. Mach. Intell.*, vol. 40, no. 8, pp. 1888–1902, 2017.